Understanding friction induced damping in bolted assemblies through explicit transient simulation

Guillaume Vermot Des Roches, Etienne Balmès

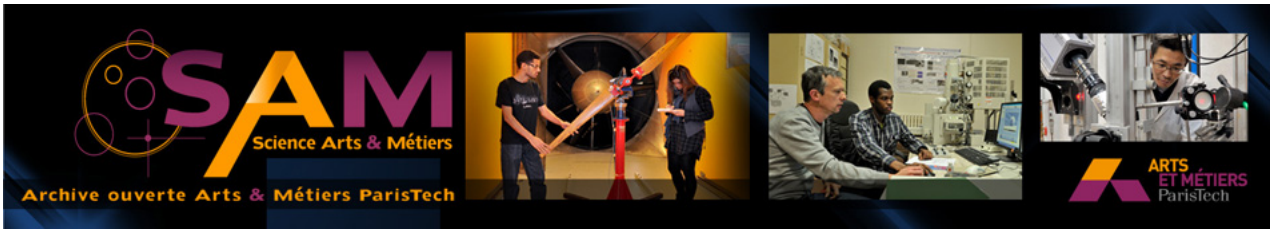

Understanding friction induced damping in bolted assemblies through explicit transient simulation

G. Vermot des Roches [1,2]**, E. Balmes** [2,1]
[1]SDTools
44 rue Vergniaud, F-75013, Paris, France
e-mail: **vermot@sdtools.com**

[2]Arts et Metiers ParisTech, PIMM
151 Boulevard de l'Hôpital, F-75013, Paris, France

Abstract
The design of joints is seeing increased interest as one of the ways of controlling damping levels in lighter and more flexible aeronautic structures. Damping induced by joint dissipation has been studied for more than a decade, mostly experimentally due to the difficulty of simulating large structures with non-linearities. Experimentally fitted meta-models were thus used for damping estimation at design stage without a possible optimization. The aim of this paper is to demonstrate that damping estimation using local friction models is feasible and that it can be usable for design. The simulation methodology is based on an explicit Newmark time scheme with model reduction and numerical damping that can be compensated for the modes of interest. Practical simulation times counted in minutes are achieved for detailed models. The illustration on a lap-joint shows how simulations can be used to predict the amplitude dependence of modal damping, answer long standing questions such as "does the modeshape change?" or analyze the evolution of pressure fields during a cycle.

1 Introduction

Optimization of the performance of aeronautic structures leads to lighter and typically more flexible designs. Meeting dynamic performance targets thus becomes more difficult and controlling damping is of a clear interest. Since materials used in aeronautic construction are typically lightly damped, design work must focus on junctions using either friction or viscoelasticity as the physical damping mechanism. Damping in jointed structure has been the focus of much research on experimental characterization and meta-model descriptions of joint behavior (see [10, 12, 13] to cite a few). The present work is part of the global MAIAS project, which seeks to demonstrate that the damping induced by joint dissipation is measurable and that its optimization by numerical prototyping is feasible.

Numerical prediction of friction induced damping in joints is considered a challenging computation [5, 12, 9], so that discussion of the exact procedure is a first objective of this paper.

Several resolution strategies can be found in the literature to study assembled structures with non-linear joints: non-linear analysis searching for specific solutions (harmonic balance, multiple scales, homotopy), continuation methods based on the underlying linear analysis (nonlinear normal modes, complex nonlinear modal analysis), or direct transient simulations. The latter will be retained for its simplicity and generality, but the need for proper analysis tools is then critical. The second objective of the paper is thus to show how simulations can be used to predict the amplitude dependence of modal damping, answer long standing questions such as "does the modeshape change?" or analyze the evolution of pressure fields during a cycle.

The trade-off between simulation time and accuracy is oriented towards speed regarding design in early design phases. To be usable in this purpose, it is further chosen to use physical models based on a local description of contact and friction. This specificity allows a finer analysis of the structure evolution over time and richer information can be exploited.

The explicit Newmark scheme, presented in section 2.1, was retained due to its cheaper cost allowing quick non-linear simulations with small time steps over relatively long times. Numerical damping is introduced to improve the behavior with no impact in the bandwidth of interest. The contact and friction modelling strategy is presented in section 2.2.

Section 2.3 then shows that model reduction preserving global system modes, compatible with the explicit integration and retaining detailed physical models of contact can be introduced. Reference modal states are then introduced as they will be used as analysis tools and to compensate for numerical damping when needed.

As an illustration a lap-joint model is presented in section 3.1. In section 3.2, numerical estimation of frequency and damping properties as function of bolt pre-stress and amplitude are shown to reproduce classic experimental observations.

Section 3.3 then seeks to properly characterize the evolution of frequency and modeshape over a cycle. The effect of local structural deformations is analyzed in section 3.4 and shown to be the reason of damping saturation and frequency decrease patterns.

2 Explicit transient simulations of structures with local non-linearities

2.1 The explicit Newmark scheme, implementation and properties

Newmark time integration is a classical scheme in the field of structural dynamics for transient simulation applications [11]. The time space is discretized by finite differences, and the Newmark quadrature under explicit conditions provides a rule of evolution from a known system state. Knowing the state at time t_{n-1}, the new state at time t_n is for explicit conditions

$$\{q_n\} = \{q_{n-1}\} + h\{\dot{q}_{n-1}\} + \frac{h^2}{2}\{\ddot{q}_{n-1}\} \tag{1}$$

$$\{\dot{q}_n\} = \{\dot{q}_{n-1}\} + h(1-\gamma)\{\ddot{q}_{n-1}\} + h\gamma\{\ddot{q}_n\} \tag{2}$$

where $h = t_n - t_{n-1}$ is the time step, $\{q_n\}$ the system displacement field at time t_n, time derivatives are denoted by dot superscripts. γ is the classical Newmark second quadrature parameter, the first one, usually noted β is null in explicit configuration.

The quadrature rules can then be combined to the mechanical equilibrium equation

$$[M]\{\ddot{q}_n\} + [C]\{\dot{q}_n\} + [K]\{q_n\} = \{f_{c_n}\} + \{f_{NL_n}\} \tag{3}$$

noting respectively $[M]$, $[C]$ and $[K]$ the mass, damping and stiffness matrices obtained by a finite element discretization of the system, $\{f_{c_n}\}$ the linear external forces applied to the system, and $\{f_{NL_n}\}$ the internal and external non-linear forces applied to the system, that are state and time dependent.

Equation (1) is used to build displacement at the new step. The combination of the mechanical equilibrium (3) and velocity expression (1) are used to build acceleration and velocity. The explicit etiquette is given since there is no correction phase. In the presence of non-linearities, the direct resolution does not hold due to the dependence of the non-linear forces on velocity. To keep an explicit scheme, one introduces a velocity predictor based on the expression of the half-step velocity appearing in the expression of $\{q_n\}$,

$$\{\dot{q}_n^*\} = \left\{q_{n-1/2}\right\} = \{\dot{q}_{n-1}\} + \frac{h}{2}\{\ddot{q}_{n-1}\} \tag{4}$$

so that $\{q_n\} = \{q_{n-1}\} + h\{\dot{q}_n^*\}$. This velocity predictor allows the computation of the non-linear forces and the explicit resolution of acceleration assuming $\{\dot{q}_n\} \simeq \{\dot{q}_n^*\}$. The velocity field is finally updated using (1) and the new step acceleration.

The resulting time integration scheme is synthetized in figure 1. It is very compact and does not perform convergence checks nor internal iterations.

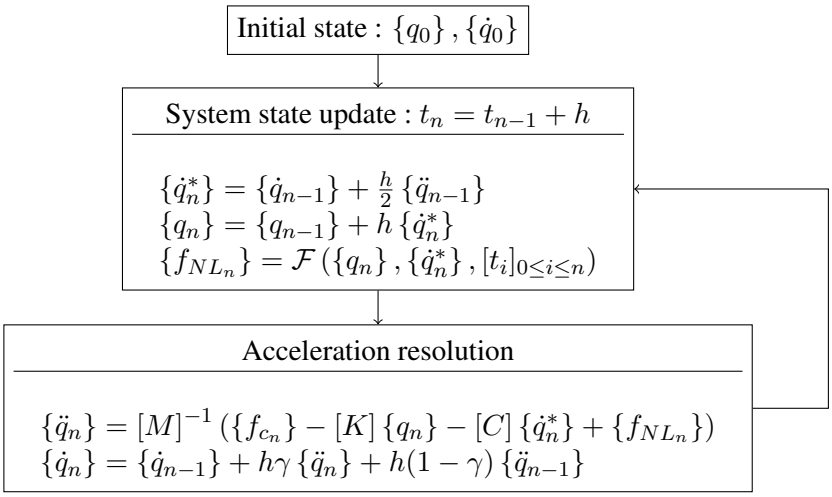

Figure 1: Implementation of an explicit non-linear Newmark time integration scheme.

The resolution approaches the mechanical equilibrium, that is not met in general. In the presence of non-linear forces, the approximation is function of the discrepancy between $\{\dot{q}_n^*\}$ and $\{\dot{q}_n\}$. For small time steps in the scales needed regarding the scheme stability, this approximation is often acceptable.

The explicit quadrature (1) makes the scheme only conditionally stable [11] for time steps verifying for all system modes of pulsation ω_j

$$\omega_j^2 h^2 \leq \frac{4}{(\gamma + \frac{1}{2})^2} \text{ and } \gamma \geq \frac{1}{2} \tag{5}$$

This condition is often adapted into the Courant, Friedrichs and Lewy condition, that proposes to bound ω_{max} using the time needed for a dilatational stress wave to traverse the smallest element of the mesh.

The scheme presented in figure 1 features a single linear system resolution based on the mass matrix. Without internal time step iteration the computational cost of a time step becomes cheap. The use of mass lumping techniques [17] allows computing mass matrices with diagonal topology thus making trivial the resolution of the new acceleration.

With a scheme featuring only matrix-vector operations the cost of a time step can take less than 10ms on recent workstations for systems with 30,000 DOF (using SDT [1] and its non-linear module). The trade-off between the small time step required for stability and the computational cost of a time step then makes this methodology attractive for some applications. In particular, for transient contact friction simulations, implicit formulations already require small time steps to converge so that the choice of an explicit scheme quickly becomes advantageous.

The lack of mechanical equilibrium tends to generate high frequency waves in the system much above the frequency range of interest and with wavelengths close to mesh size. A trade-off between time step and numerical damping must thus be considered. The scheme properties extracted from its expression in terms of evolution operator in the linear case gives estimates in terms of amplitude and periodicity errors [11]. For linear models, a direct numerical modal damping ratio $\zeta_{\gamma j}$ can be computed for a mode at pulsation ω_j,

$$\zeta_{\gamma j} = \frac{-1}{2h\omega_j} \ln\left(1 - \left(\gamma - \frac{1}{2}\right)\omega_j^2 h^2\right) \tag{6}$$

Using $\gamma > \frac{1}{2}$ puts more weight on the new step in the evaluation of velocity (1) and generates numerical damping changes with frequeny and time step. For the explicit Newmark scheme, the higher h or γ, the higher the damping ratio. Figure 2 illustrates that the frequency at which critical damping is reached can be controled with the time step while the peak damping depends on the value of γ.

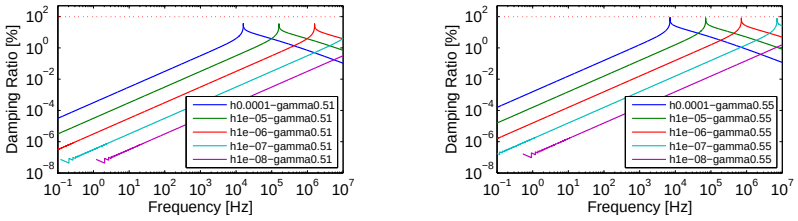

(a) $\gamma = 0.51$ (b) $\gamma = 0.55$

Figure 2: Numerical damping ratio induced by the Newmark scheme as function of the time step h and γ.

For a given application, one should thus choose parameters such that numerical damping does not interact with predictions of interest. Typical targets would be to have equivalent modal damping below 0.01% for frequencies one or two decade above the last frequency of interest. Using compensation discussed in section 2.3.2 is an alternative.

2.2 Contact and friction modelling adapted to an explicit scheme

Contact and friction modelling for finite element models is a complex task. The surface topology to account for contact should be at the scale of asperities responsible for roughness, but this scale is orders of magnitude smaller than the current computational possibilities using finite elements. One must then approach the surface behavior using the mean plane of the solid finite element interface.

Several modelling strategies exist in the literature, as reviewed by the authors in [16], that can be equivalent in terms of resulting system dynamic properties. Bograd *et al.* [4] provide a review of the strategies that have been used for joint modelling.

Contact enforcement under the Signorini condition is classically written for a finite element model

$$\begin{cases} g(x_j) \geq 0 \\ p(x_j) \geq 0 \\ g(x_j) \cdot p(x_j) = 0 \end{cases} \tag{7}$$

where for a given contact integration point x_j, $g(x_j)$ is the gap or clearance to its matched location to the surface in regard, and $p(x_j)$ is the contact pressure. Under the law (7) the surface non-interpenetration at the contact points is guaranteed with the existence of the repulsive forces. In practice contact points are chosen on one of the two surfaces, named master, the second surface being named slave.

The gap is computed as the relative displacement between the contact point considered (master) to the facing slave surface along the normal considered at that point , namely $N(x_j)$,

$$g(x_j) = N(x_j).(q(x_{j/p}) - q(x_j)) - g_0 \tag{8}$$

with $x_{j/p}$ the localization of the contact point projected on the slave surface. The computation of the gap only involves finite element shape functions interpolations from the displacement field. The gap vector can thus be expressed using a linear observation operator $[C_N]_{N_c \times N}$ with N the number of DOF and N_c the number of contact points,

$$\{g\}_{N_c \times 1} = [C_N]_{N_c \times N} \{q\}_{N \times 1} \tag{9}$$

The generalized force resulting from the pressure field $p(x_j)$, with the gap defined at each contact point, is defined as

$$\{\hat{q}\}^T \{f_N\} = \int_\Gamma \hat{u}(\hat{q}) N p dS \simeq \sum_e \sum_j \{\hat{u}(\hat{q})\}^T \{N\} p(x_j) w_j^{(e)} J^{(e)}(x_j) \tag{10}$$

where $\{f_N\}$ is the generalized contact force, p the contact pressure, $\{\hat{q}\}$ a virtual displacement, $\{q\}$ the displacement, $x_j^{(e)}$ are the integration points of current element e, $J^{(e)}(x_j)$ the Jacobian of the shape transformation (surface associated to each integration point) and $w_j^{(e)}$ the weighting associated with the integration rule of element e.

The use of observation matrix $[C_N]$ is also possible, so that in practice the generalized contact force is expressed as function of the local contact pressure as

$$\{f_N\}_{N\times 1} = [C_N]^T_{N\times N_c} \left\{ w_j^{(e)} J^{(e)}(x_j)\, p(x_j) \right\}_{N_c \times 1} \tag{11}$$

Similar developments can be performed for the relative tangential displacement, sliding velocity and generalized friction force, noting $[C_T]_{2N_c\times N}$ the relative displacement observation matrix. A fully detailed numerical implementation under the present conventions is provided in [14].

Using an explicit scheme as in figure 1, contact enforcement can be considered as an alteration of the acceleration field $\{\ddot{q}_{n-1}\}$ to avoid interpenetration occurrences for $\{q_n\}$. Assuming interpenetration occurs for $\{q_n\}$, one searches $\{\delta q_n\}$ so that

$$[C_N]\left(\{q_n\} + \{\delta q_n\}\right) = 0 \tag{12}$$

Several solutions exist, one being to repel both slave and master surfaces by half the interpenetration

$$\{\delta q_n\} = -\frac{1}{2} [C_N]^T [C_N] \{q_n\} \tag{13}$$

Using (1), relation (12) can be expressed as a non-linear force applied at step $n-1$ function of $\{q_n\}$

$$\{f_{NLn-1}(q_n)\} = \frac{2}{h^2} [M] \{\delta q_n\} = -\frac{1}{h^2} [M] [C_N]^T [C_N] \{q_n\} \tag{14}$$

Assuming a linear pressure-gap relationship

$$p(x_j) = k_c(x_j) g(x_j) \tag{15}$$

the expression of the generalized contact force (11) leads to an equivalent contact stiffness $k_c(x_j)$

$$k_c(x_j) = \frac{1}{2 w_j h^2} \left[\backslash \{C_{Nj}\} [M] \{C_{Nj}\}^T \backslash \right] \tag{16}$$

Although not directly applicable to the non-linear Newmark scheme as an acceleration correction should be computed, the existence of an optimal finite stiffness when exactly enforcing the Signorini condition is interesting. Using a higher contact stiffness (16) would generate rebounds and make the solution diverge. This critetion is different from the Courant condition (5) which applies within the mesh.

The choice of a functional (or penalized) unilateral contact law with a linear pressure-penetration law (15) is then justified as a starting choice regarding this paper scope. In practice one calibrates the contact stiffness to be under the optimal (16) and in the saturated area regarding the dynamical behavior [16]. The value of $k_c = 10^8 MPa/mm$ was used in practice.

Modelling of friction has the same difficulties as contact, but functional modelling is more complex to apprehend. Friction phenomena at the scale of multibody dynamics generate various and complex effects, such

as hysteresis, dwell, *etc*. This has led some authors to propose analytical functional friction models implementing all these phenomena at a macroscopic level (or meta-models) using experimental characterization. The Iwan model [13] is an example.

The strategy retained here involves simpler laws that are based on the expected physical behavior, thus belonging to the class of heuristic models, as for example detailed in [4]. The main advantage of local heuristic models is the ability to localize friction dissipation in the joints, which is of critical interest for design studies.

The frictional memory is represented by an internal state $z(x_j, t)$ that can be identified as the tangential displacement induced by the sliding velocity when non-zero, and a constant otherwise. If non-sliding, an elastic force $f_{TS}(x_j, t+h)$ of stiffness k_t is opposed to the relative tangential displacement.

$$f_{TS}(x_j, t+h) = k_t \left(\{C_{Tj}\}^T \{q(t+h)\} - z(x_j, t) \right) \tag{17}$$

At a given contact point x_j, the friction constraint for a sticking point is thus expressed as

$$\begin{cases} |f_{TS}(x_j, t+h)| \leq \mu p(x_j, t+h) \\ f_T(x_j, t+h) = f_{TS}(x_j, t+h) \\ z(x_j, t+h) = z(x_j, t) \end{cases} \tag{18}$$

The friction force is bounded by the friction coefficient μ, so that once the sliding force limit $\mu p(x_j, t+h)$ is hit, sliding is initiated and directed opposite to the sliding velocity $w_s(x_j, t) = [C_T] \{\dot{q}(t)\}$. The internal state $z(x_j, t)$ is displaced with the relative sliding velocity,

$$\begin{cases} |f_{TS}(x_j, t+h)| > \mu p(x_j, t+h) \\ f_T(x_j, t+h) = -\mu p(x_j, t+h) \frac{w_s(x_j, t+h)}{\|w_s(x_j, t+h)\|} \\ z(x_j, t+h) = z(x_j, t) + h w_s(x_j, t+h) \end{cases} \tag{19}$$

The set of equations (18)-(19) define a friction law with sticking capability. Great similitudes exist with meta-models, as each contact point could be considered as a cell of the macroscopic models usually developed. Values of $k_t = 10^8 MPa/mm$ and $\mu = 0.3$ were chosen for the study.

2.3 Using system modes in transient simulations: reduction and modal damping

2.3.1 Reduction strategy

In this paper application the model size is not an issue, the reduction however allows controlling the maximum system frequency and confining the spurious high frequency waves in the contact area.

Base reduction techniques have been assessed in the literature [6, 7] for linear models. Model reduction in the presence of non-linearities raises some issues as modal decoupling is not possible in general. Methods for non-linear simulations exist since the 70's using the classical concepts of mode superposition and substructuring [2], with a specific need for restitution at each step to compute the non-linear forces.

For structures with local non-linearities, one can build a hybrid model coupling a non-reduced part supporting the localization of the non-linearity and a reduced part behaving linearly. The reduction method chosen for the present work is based on the Component Mode Tuning method (CMT) [15] that ensures the convergence of the system dynamics of interest, and the generation of very compact systems while keeping a sparsity independent from the interface size.

One here considers two elastically coupled disjoint components 1 (N_1 DOF) and 2 (N_2 DOF), Rayleigh-Ritz bases non zero for a single component

$$\{q\}_{(N_1+N_2)\times 1} = [T_R] \{q_R\}_{(n_1+n_2)\times 1} = \begin{bmatrix} T_1 & 0 \\ 0 & T_2 \end{bmatrix} \begin{bmatrix} q_{R1} \\ q_{R2} \end{bmatrix} \tag{20}$$

and the dynamic stiffness that can be decomposed as the sum of independent component contributions Z_i and an interface coupling matrix Z_I

$$[Z]_{(N_1+N_2)\times(N_1+N_2)} = [Z_{el}] + [Z_I] = \begin{bmatrix} Z_1 & 0 \\ 0 & Z_2 \end{bmatrix} + \begin{bmatrix} Z_{I11} & Z_{I12} \\ Z_{I21} & Z_{I22} \end{bmatrix} \tag{21}$$

In the general case, component decoupling can be performed by selecting a layer of elements representing the coupling interface [14], thus cutting a system apart, as considered in this paper. If no internal nodes are contained in the element layer, the formalism of equation (21) is still valid.

In this formulation, continuity is always verified since (20) expresses motion using the full model FEM coordinates. The reduced dynamic stiffness matrix $[Z_R]$ is written

$$[Z_R]_{(n_1+n_2)\times(n_1+n_2)} = \begin{bmatrix} T_1^T Z_1 T_1 & 0 \\ 0 & T_2^T Z_2 T_2 \end{bmatrix} + \begin{bmatrix} T_1^T Z_{I11} T_1 & T_1^T Z_{I12} T_2 \\ T_2^T Z_{I21} T_1 & T_2^T Z_{I22} T_2 \end{bmatrix} \tag{22}$$

Unlike the Craig-Bampton method which needs complete interface description to enforce continuity, the CMT method only needs to focus on selecting retained shapes relevant for other objectives. Reduction bases $[T_k]_{N_k\times n_k}$ can be generated using the restriction of the assembled system modes on each component, $\left[\Phi_{|k}\right]$. In such case, the reduced system will give the exact result [15]. The subspaces generated for each component are effectively coherent with the assembled system subspace and all interface motion is well described since by definition all the desired motion is retained in the basis.

In the general case where a layer of elements was extracted to decouple the components, mass coupling terms exist in (22) and mass lumpiness is lost, altering the performance of the explicit Newmark scheme.

This issue is resolved by locally redistributing the mass coupling terms between components. To explain this operation one has to consider the interface DOF i that contains the coupling terms between components 1 and 2. In practice these DOF are reduced and are here considered belonging to the component 1 DOF. This formalism is then compatible in the case where a component is not reduced. One then splits the DOF vector noting q_{1c} and q_{2c} the complementary (or internal) DOF of both components and q_i their common interface DOF,

$$\{q\} = \begin{Bmatrix} q_{1c} \\ q_i \\ q_{2c} \end{Bmatrix} \tag{23}$$

The interface DOF bear the mass coupling between components, so that the mass matrix can be written

$$[M] = \begin{bmatrix} M_{1cc} & M_{1ci} & 0 \\ M_{1ic} & M_{1ii} + M_{2ii} & 0 \\ 0 & M_{2ci} & M_{2cc} \end{bmatrix} \tag{24}$$

where each component mass matrix is split between the interface DOF i and complementary DOF c.

The mass redistribution consists in assuming that one of the components bears all the mass contained in the interface, thus considering matrices $\hat{M}_1$ and $\hat{M}_2$ instead of M_1 and M_2, defined as

$$\hat{M}_1 = \begin{bmatrix} M_{1cc} & M_{1ci} \\ M_{1ic} & M_{1ii} + M_{2ii} \end{bmatrix} \text{ and } \hat{M}_2 = \begin{bmatrix} 0 & M_{2ic} \\ M_{2ci} & M_{2cc} \end{bmatrix} \tag{25}$$

Noting $\tilde{M}_{2ic}$ and $\tilde{M}_{2ci}$ the expansion of respectively matrices M_{2ic} and M_{2ci} from the DOF set i to the DOF set $(1c, i)$, the mass matrix can be written

$$[M] = \begin{bmatrix} \hat{M}_1 & 0 \\ 0 & M_{2cc} \end{bmatrix} + \begin{bmatrix} 0 & \tilde{M}_{2ic} \\ \tilde{M}_{2ci} & 0 \end{bmatrix} \tag{26}$$

If the initial mass was lumped, terms $\tilde{M}_{2ic}$ and $\tilde{M}_{2ci}$ are null so that the expression of the mass matrix does not contain coupling terms between components 1 and 2. An orthonormalization procedure operated for each component will thus yield a diagonal mass matrix in the general case.

No approximation is performed when using the representation of the mass matrix (26). The only change is that in the basis T_1 used in (20) which is made orthogonal to $\hat{M}_1$ to obtain a diagonal mass for fast explicit integration. This however does not alter the corresponding subspace and thus has no impact on the solution.

2.3.2 Using modal damping and sensing in transient simulations

The application of modal damping in transient simulations has been presented by the authors in [3]. It consists in an implicit expression of the identified full damping matrix in the physical space by the inversion of the projection of the damping matrix $[\mathcal{C}]$ in the modal subspace $[\Phi]$

$$[\mathcal{C}] = \left[\backslash 2\zeta_{mj}\omega_{j\backslash}\right] = [\Phi]^T [C_M] [\Phi] \tag{27}$$

noting that a pseudo inverse of a mass normalized modal basis can be directly obtained as $[\Phi]^+ = [M][\Phi]$. The application of the physical modal damping matrix to a velocity field can then be expressed as a series of matrix-vector product compatible with a numerical implementation

$$[C_M]\{\dot{q}_n\} = \left([M][\Phi]\left(\left[\backslash 2\zeta_{mj}\omega_{j\backslash}\right]\left([\Phi]^T[M]\{\dot{q}_n\}\right)\right)\right) \tag{28}$$

Using the identified numerical modal damping coefficients (6), one can then cancel the effect on the modes of interest by using $\zeta_{mj} = -\zeta_{\gamma j}$ in (28). The cancellation is exact for linear models and an approximation is made for non-linear models.

The use of numerical damping is thus possible with a control on the dynamics of interest. In the same manner, use of mass scaling techniques, that are common for quasi-static simulations, could also be used along with a compensation to control the modal inertias of the modes of interest.

Using the same relation (27), one sees that the real mode contribution to the mechanical energy can be recovered [14]. Noting the response as a linear combination of the system real modes

$$\{q(t)\} = \sum_j \alpha_j(t)\{\phi_j\} + \{q_R(t)\} \tag{29}$$

one identifies the coefficients of modal contribution coefficients $\alpha_j(t)$ as

$$\begin{cases} \alpha_j(t) = \{\phi_j\}^T [M]\{q(t)\} \\ \dot{\alpha}_j(t) = \{\phi_j\}^T [M]\{\dot{q}(t)\} \end{cases} \tag{30}$$

The mechanical energy $E_{mj}(t)$ associated to mode j contribution can then be computed as

$$2E_{mj}(t) = 2E_{strain_j} + 2E_{kin_j} = \omega_j^2\alpha_j^2(t) + \dot{\alpha}_j^2(t) \tag{31}$$

This indicator provides the transient modal mechanical energies that can be summed to obtain the total mechanical energy expressed in the direction of the system modes.

3 Estimation and analysis of the time varying modal properties of a lap-joint model

3.1 Presentation of the lap-joint model

The lap-joint model considered is presented in figure 3. It is a classical benchmark in the literature due to its simplicity [4]. The short flange has a length of $86mm$ with an overlapping length of $50mm$ with the long flange of $270mm$. The flanges have a width of $24.8mm$ and a thickness of $4.7mm$.

The bolt is modelled using rigid rings representing the bolt head of diameter $10.5mm$ and a beam representing the bolt member of core diameter of $7mm$. A quadratic mesh with hexahedron elements was chosen to improve convergence of contact fields.

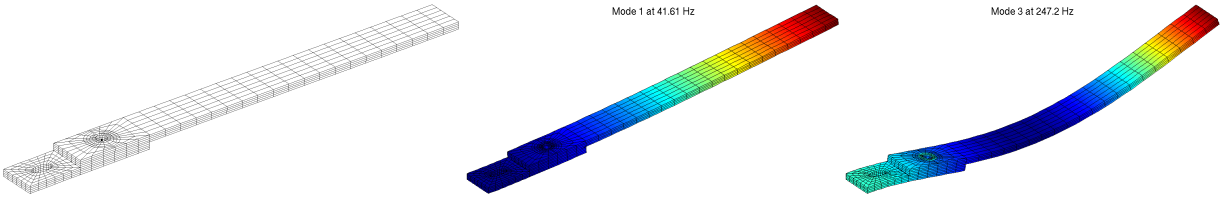

Figure 3: A simple lap-joint model with its first two bending modes at 41.61Hz and 247.2 Hz.

The resolution of non-linear static states is generally difficult and requires *ad-hoc* treatment for large structures with multiple contacts. The strategy chosen is to perform quasi-static transient loading of the structure using the method presented in section 2, with a control of the global structural deformation. Bolt tightening is performed by applying a compression force on one beam element with released compression DOF.

The tightening operation from a zero deformation state is possible using short pseudo time steps (or large force increments) by overly damping the structure. The transient simulation span is kept long enough so that contact fields stabilize. Once contact fields are stabilized, one here performs a direct static linear resolution based on the system tangent state.

A control is performed on the contact point statuses to check that the tangent state did not vary. If contact statuses varied a loop is performed so that a new transient quasi-static simulation is launched with the new structural deformation. The static response of the linear part of the structure due to the bolt loading is then obtained very efficiently. The resulting loading is presented in figure 4.

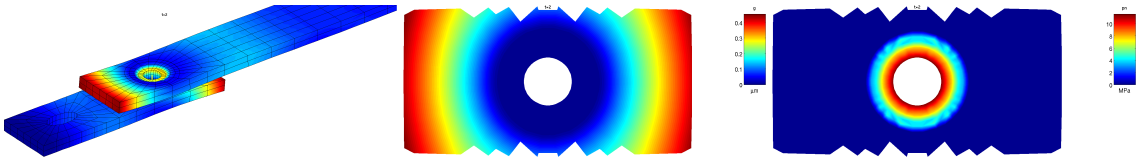

.

Figure 4: Static bolt pre-stress, deformation field, gap (max $0.4\mu m$) and pressure fields (max $15MPa$))

For dynamic computations, the lap-joint model is reduced using the methodology of section 2.3. The chosen reduced and kept areas for the lap-joint model are presented in figure 5left. The kept area has to be large enough to allow a clean response of the structure to the wave propagations generated by the contact impacts. The complete area containing the contact part had to be kept, since the structure is rather simple.

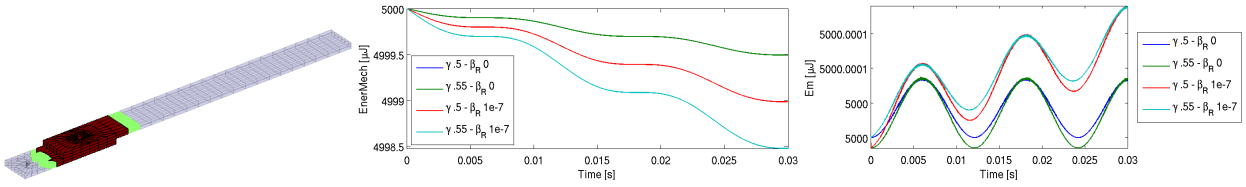

.

Figure 5: Left: the kept area chosen for the lap-joint model (in red), reduced part (in blue) and reduced coupling element layer (in green). Middle: Effect of numerical damping on the mechanical energy evolution (linear case). Right: Mechanical energy with scheme compensation (linear case)

The numerical damping compensation procedure developed in section 2.3 has been tested for the linear case (fixed contact surface) along with the use of a global Rayleigh damping in stiffness ($[C_R] = \beta_R [K]$) set

to damp higher frequencies. Scheme and Rayleigh damping generate a dissipation, figure 5middle. The damping cancellation strategy allows recovering the undamped energy patterns, seen in figure 5right. A slight difference occurs for the case of Rayleigh damping, a possible cause being the numerical round-off errors due to the use of the stiffness matrix on the velocity signals.

3.2 Estimation of modal properties as function of bolt pre-stress and amplitude

For a non-linear system submitted to varying apparent stiffness (plasticity, geometric stiffness, contact), the system modes vary over time, as they are defined as tangent to a certain state of the system. Frequency evolution tracking is usually performed in tests by the use of filtering techniques, and possibly based on signal processing techniques, like the Hilbert transform [8].

The apparent frequency of a non-linear cycle can also be seen as a synthesis of a system instantaneous states with possibly significant state variation. The measurement method presented by Heller *et al.* [12] performs modal identification by taking into account amplitude dependence of frequency and damping of the poles. In general the assumption is made that the mode shape does not vary.

Based on single cycle simulations of free decay, a detailed analysis of the system evolution over time is possible. Initialization is here performed using an initial velocity in the direction of the first mode shape.

The extraction of modal properties has been kept very simple in the study presented. Frequency has been estimated using direct cycle durations based on the interpolated tops of the kinetic energy signal. Damping ratios have been estimated by direct decrement method using the mechanical energy values at the cycle starting point E_{m0}, and ending point E_{mj},

$$\zeta_j = \frac{1}{4\pi} \ln\left(\frac{E_{m0}}{E_{mj}}\right) \tag{32}$$

A sample design of experiment study has been performed as function of bolt pre-stress and amplitude to quantify the interesting parameter ranges and test the capability of the simulation strategy. The trends observed presented in figure 6 are rather similar to experimentally observed behavior [12].

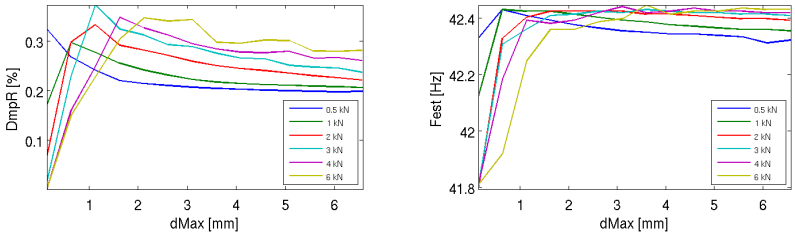

Figure 6: Frequency and damping evolution as function of bolt pre-stress (colored curves) and vibration amplitude $dMax$ for the first bending mode of the lap-joint model.

The modal damping ratio first shows an increase with a local maximum as function of the amplitude, with different values and location as function of the pre-stress.

The frequency shows a decreasing trend as function of amplitude. An initial increase from the static state is observed that is not common experimentally. As it occurs for low amplitudes, it may be difficult to attain in testing and may yield an updating bias in correlation. An investigation of the frequency evolution causes is presented in section 3.3 for the case with a pre-stress of $4kN$ and the maximum amplitude, here $6.5mm$.

3.3 Instant frequency. Is the modeshape constant ?

This section seeks to answer a recurrent question in joint damping studies as to whether the modeshapes are changing or not.

A basic criterion is given by the Rayleigh quotient which as proposed in [9] can be used to estimate instantaneous frequencies

$$\omega_j^2(t) = \frac{\{q(t)\}^T [K] \{q(t)\}}{\{q(t)\}^T [M] \{q(t)\}} \tag{33}$$

It must be noted that the transient deformation fields are expressed as the sum of a static state and a vibration field $\{q(t)\} = \{q_0\} + \{\tilde{q}(t)\}$. The Rayleigh quotient estimation is based on the vibration part of the displacement, so that the static contribution should not be taken into account. Cross product terms subsist nevertheless in the Rayleigh quotient,

$$\omega_j^2(t) = \frac{\{\tilde{q}(t)\}^T [K] \{\tilde{q}(t)\} + 2\{\tilde{q}(t)\}^T [K] \{q_0\}}{\{\tilde{q}(t)\}^T [M] \{\tilde{q}(t)\} + 2\{\tilde{q}(t)\}^T [M] \{q_0\}} \tag{34}$$

Figure 7left presents the result of this evaluation over time. For low displacement (starting point, half and full cycle), the denominator becomes very small and it is unclear that the value can be used. For sufficient deflection ($1/4$ and $3/4$ cycles shown as dotted lines) two distinct frequencies clearly appear. This dissymmetry seems to indicate that the system behavior depends on the deflection direction.

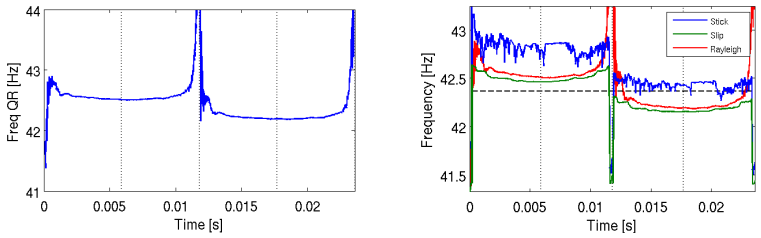

Figure 7: Left: Rayleigh quotient evaluation as function of time, over a cycle. Right: comparison with the instant frequencies considering either sticking coupling or not. Marks correspond to the 4 cycle quarters.

A second strategy to estimate instant frequencies is the use of the tangent modes based on the transient trajectory [14]. Figure 7right presents the frequency estimation for different tangent state formulations either using sticking conditions or not. The definition of the sticking condition is here biased by the lack of equilibrium between the velocity and the non-linear forces and does not seem to be easily exploitable.

The evaluation of the instant frequencies with the free sliding condition is smoother and the mean instant frequency is very close (0.02Hz) to the full cycle frequency based on its duration and represented by the black dashed line in figure 7right. The Rayleigh quotient estimation (34) is also close to the instant sliding frequencies.

The observed frequency variations indicate that the system properties evolve over time. This pattern can indeed be related to the fact that the system does not vibrate on the exact initial mode shape. The use of the modal sensors presented in section 2.3 allows the computation of the first mode mechanical energy contribution, using equation (31). The ratio of the total mechanical energy to the modal mechanical energy is thus an indicator of the mode shape variation over time.

Figure 8a first presents the evolution of the total mechanical energy. The dissipation rate is not constant, for low velocity states (at large amplitudes) no dissipation occurs. A global stuck state is generated at the velocity sign reversal and explains the plateaus on the mechanical energy evolution.

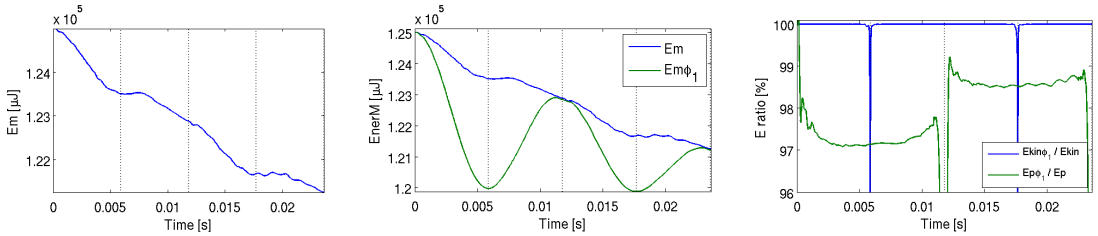

(a) Total mechainical energy

(b) Total and modal mechanical energies

(c) Modal strain and kinetic energy ratios versus total

Figure 8: Mechanical energy indicators computed over a cycle of the first flexion of the lap-joint model.

The mechanical energy associated to the first mode in figure 8b shows a clear decrease as function of the deflection amplitude, and seems to be close to the global energy at low deflections. This behavior can thus be related to a contact area variation at high deflection.

It is interesting to note that the discrepancies between the modal mechanical energy and total mechanical energy only occur when the strain energy is high. Figure 8c illustrates this pattern by plotting the kinetic and strain energy ratio of the modal participation versus the total energies. It can thus be seen that the kinetic energy ratio (when defined, outside very low ranges of values) is constantly close to 1. The strain energy ratio (when defined) however decreases with time and shows a 3% variation.

The fact that the kinetic energy ratio keeps close to 1 tells that the velocity field remains close to the original mode shape, although the local contact configuration alters the displacement field and thus locally the mode shape. The modeshape is thus invariant for kinetic energy, or experiments which typically use a related norm, and variable for strain energy. Hence the long standing debate on the variation of modeshapes.

3.4 Localizing the shape variations

Shape differences are localized in the areas with contact state variation, since the shape cannot change in the reduced area due to the reduction. The base Modal Assurance Criterion (MAC) should then not detect the shape variations. The use of a K-MAC would be more relevant.

Modeshape discrepancies are plotted for the non-reduced area in figure 9. Figures 9a-g present the first mode shape when contact is closed at the clamped side (left of the figure). The differential displacement thus mainly consists in a correction to the tip of the upper joint member to avoid interpenetration.

The opening between the members at the free side also varies with time as the iso-values used for displacements of lower amplitudes move, indicating a strain of the bore. Figures 9h-o present the first mode shape when contact is closed at the free side (right of the figure). Identical observations can be done.

The root cause of the shape variation can only be in this case the variation of the contact and friction forces. The fact that instant frequencies with free sliding conditions provide similar evolutions to the instant Rayleigh quotient as seen in section 3.3 indicates that the contact forces play a major role.

The contact field variation is illustrated in figure 10, that dipslays iso-values of contact pressures over time. The effective contact surfaces can then be visually observed in a coarse manner.

It can be observed for large deflection instants, figures 10d-e and 10h-n, that the contact pressure field varies at the bore, with an ovalization of the contact field, increasing contact in the transverse direction and decreasing contact in the longitudinal direction. The contact area thus also varies outside the joint extreme sides that come into contact quickly due to bending.

To quantify the bore strain effect, one computes the effective (or closed) contact surface $\mathcal{S}_c(t)$,

$$\mathcal{S}_c(t) = \sum_{x_j \in \mathcal{C}(t)} w_j^{(e)} J^{(e)}(x_j) \tag{35}$$

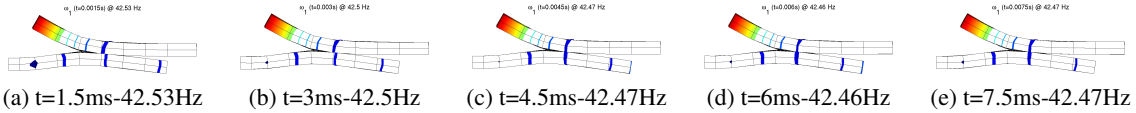

(a) t=1.5ms-42.53Hz (b) t=3ms-42.5Hz (c) t=4.5ms-42.47Hz (d) t=6ms-42.46Hz (e) t=7.5ms-42.47Hz

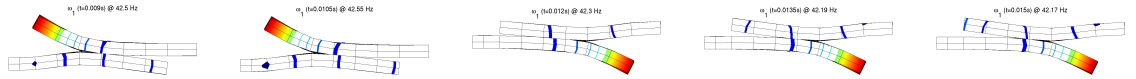

(f) t=9ms-42.5Hz (g) t=10.5ms-42.55Hz (h) t=12ms-42.3Hz (i) t=13.5ms-42.19Hz (j) t=15ms-42.17Hz

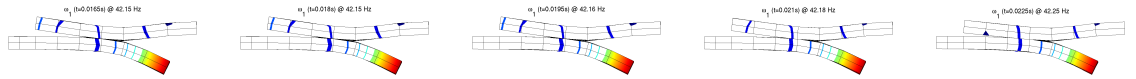

(k) t=16.5ms-42.15Hz (l) t=18ms-42.15Hz (m) t=19.5ms-42.15Hz (n) t=21ms-42.18Hz (o) t=22.5ms-42.25Hz

Figure 9: Instant mode #1 shape variation over a cycle, equally subsampled points over a cycle.

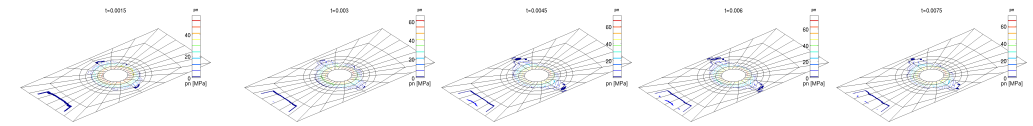

(a) Pn @ t=1.5ms (b) Pn @ t=3ms (c) Pn @ t=4.5ms (d) Pn @ 6ms (e) Pn @ 7.5ms

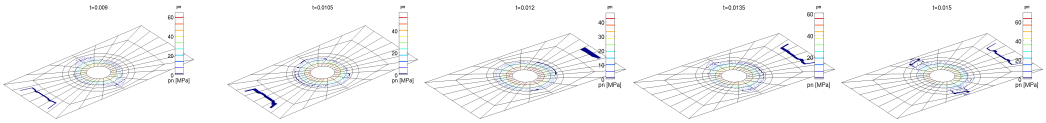

(f) Pn @ 9ms (g) Pn @ 10.5ms (h) Pn @ 12ms (i) Pn @ 13.5ms (j) Pn @ 15ms

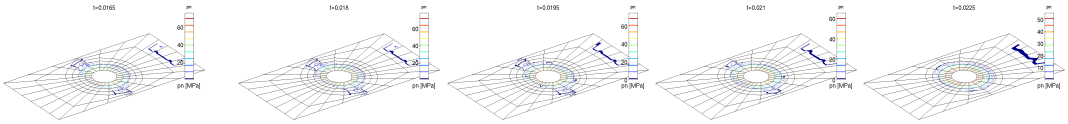

(k) Pn @ 16.5ms (l) Pn @ 18ms (m) Pn @ 19.5ms (n) Pn @ 21ms (o) Pn @ 22.5ms

Figure 10: Iso-contact pressure distribution over a cycle based on the first mode.

where notations of (10) are used and $\mathcal{C}(t) = \{x_j / p(x_j, t) > 0\}$, the ensemble of Gauss contact points in closed contact a instant t, detected by a strictly positive pressure.

Figure 11 presents the effective contact area as function of time. It can be seen that although the side closing pattern increases the total surface (seen at the very first and last instants), the contact field ovalization pattern tends to decrease the surface. As a consequence, it can be understood that although the instant frequency increases at the begining of the quarter cycles, the ovalization occurring for higher vibration amplitudes limits the phenomenon..

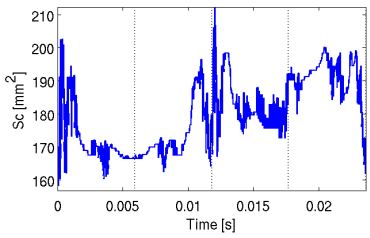

Figure 11: Effective (or closed) contact area as function of time for the cycle of maximal amplitude.

The saturation patterns observed in figure 6 are here explained by the ovalization of the contact field linked to the bore strain. This deformation is limited for low amplitudes where the contact closing at the lap joint sides is predominant, yielding an increase of the cycle frequency. The associated damping caused by local sliding in the bore vicinity also increases with the amplitude and the increasing sliding velocities.

For a given amplitude threshold, the bolt applies loads opposed to the beam bending in the bore area that generate local deformations. This causes a decrease of the effective contact surface and saturates the frequency increase with amplitude. As contact opens in the local sliding areas dissipation gets saturated despite the increasing global velocity.

4 Conclusion

The paper demonstrated the ability to combine model reduction, explicit integration and compensated numerical damping to produce efficient transient computations of detailed models.

The use of local contact and friction models allows for a fine representation of the structure evolution in the dissipative areas, that can provide relevant design information. Modal sensing and instant modal properties evolution become available and provide good insight in the expression and root cause of the modal properties evolution over time.

For the lap-joint test case used as illustration, modal frequencies and damping vary significantly with amplitude. These were shown to be strongly linked to variations of the effective contact surface. In particular, the frequency decrease and damping saturation patterns were due to deformations that generate contact openings in dissipative areas. Modal energy indicators also showed that the modeshape variation is not visible in the kinetic energy while clearly seen in the strain energy.

The dependence on local deformation leads to think that dissipation will be strongly dependent on loading seen by the joint. Design work should thus insist on accurately reproducing the joint solicitation. This is compatible with the very general time integration strategy that was presented. Further work thus focuses on handling multiple joints and excited modes.

Acknowledgements

This work was partially funded by pole Astech project MAIAS whose partners are EADS, ACM, ADR, AER, JPB systeme, SOPEMEA, ARTS, CNES, ONERA and SUPMECA.

References

[1] E. Balmes, J.-P. Bianchi, and G. Vermot des Roches, *Structural dynamics toolbox 6.6 (for use with matlab)*, SDTools, Paris, France, www.sdtools.com, October 2013.

[2] K.-J. Bathe and S. Gracewski, *On nonlinear dynamic analysis using substructuring and mode superposition*, Computers & Structures **13** (1981), no. 5-6, 699–707.

[3] J.-P. Bianchi, E. Balmes, G. Vermot des Roches, and A. Bobillot, *Using modal damping for full model transient analysis*, Proceedings of the International Conference on Advanced Acoustics and Vibration Engineering (ISMA), 2010.

[4] S. Bograd, P. Reuss, A. Schmidt, L. Gaul, and M. Mayer, *Modeling the dynamics of mechanical joints*, Mechanical Systems and Signal Processing **25** (2011), no. 8, 2801 – 2826.

[5] A. Caignot, P. Ladevèze, D. Néron, and J.-F. Durand, *Virtual testing for the prediction of damping in joints*, Engineering Computations **27** (2010), no. 5, 621–644.

[6] R. Jr. Craig, *A review of time-domain and frequency domain component mode synthesis methods*, Int. J. Anal. and Exp. Modal Analysis **2** (1987), no. 2, 59–72.

[7] D. de Klerk, D.J. Rixen, and S. N. Voormeeren, *General framework for dynamic substructuring : History, review and classification of techniques*, AIAA Journal **46** (2008), no. 5, 1169–1181.

[8] M. Feldman, *Hilbert transform in vibration analysis*, Mechanical Systems and Signal Processing **25** (2011), no. 3, 735–802.

[9] H. Festjens, G. Chevallier, and J.-L. Dion, *A numerical tool for the design of assembled structures under dynamic loads*, International Journal of Mechanical Sciences **75** (2013), no. 0, 170 – 177.

[10] L Gaul and J Lenz, *Nonlinear dynamics of structures assembled by bolted joints*, Acta Mechanica **125** (1997), no. 1-4, 169–181.

[11] M. Géradin and D. Rixen, *Mechanical vibrations. theory and application to structural dynamics.*, John Wiley & Wiley and Sons, 1994, also in French, Masson, Paris, 1993.

[12] L. Heller, E. Foltête, and J. Piranda, *Experimental identification of nonlinear dynamic properties of built-up structures*, Journal of Sound and Vibration **327** (2009), no. 1-2, 183–196.

[13] Wilfred D Iwan, *A distributed-element model for hysteresis and its steady-state dynamic response*, Journal of Applied Mechanics **33** (1966), 893.

[14] G. Vermot des Roches, *Frequency and time simulation of squeal instabilities. application to the design of industrial automotive brakes*, Ph.D. thesis, Ecole Centrale Paris, CIFRE SDTools, 2010.

[15] G. Vermot des Roches, J.-P. Bianchi, E. Balmes, R. Lemaire, and T. Pasquet, *Using component modes in a system design process*, International Modal Analysis Conference (IMAC XXVIII), 2010.

[16] G. Vermot des Roches, O. Chiello, E. Balmes, and X. Lorang, *Benchmarking signorini and exponential contact laws for an industrial train brake squeal application*, Proceedings of the International Conference on Advanced Acoustics and Vibration Engineering (ISMA), 2012.

[17] O.C. Zienkiewicz, *The finite element method*, McGraw-Hill Book Company (UK) Limited, 3^{rd} edition, 1986.